COMMUNICATIONS IN COMPUTATIONAL PHYSICS
Vol. **4**, No. 3, pp. 659-674

Commun. Comput. Phys.
September 2008

Particle-in-Cell with Monte Carlo Collisions Gun Code Simulations of a Surface-Conversion H^- Ion Source

E. Chacon-Golcher[1,*] and K. J. Bowers[2]

[1] *Los Alamos National Laboratory, Los Alamos, NM 87545, USA.*
[2] *Los Alamos National Laboratory Guest Scientist, currently at D.E. Shaw & Company, New York, NY 10036, USA.*

Received 31 October 2007; Accepted (in revised version) 15 December 2007

Available online 21 April 2008

Abstract. We present an extended update on the status of a particle-in-cell with Monte Carlo collisions (PIC-MCC) gun code developed at Los Alamos for the study of surface-converter H^- ion sources. The program is fully kinetic. Some of the program's features include: solution of arbitrary electrostatic and magnetostatic fields in an axisymmetric (r,z) geometry to describe the self-consistent time evolution of a plasma; simulation of a multi-species (e^-, H^+, H_2^+ , H_3^+ , H^-) plasma discharge from a neutral hydrogen gas and filament-originated seed electrons; full 2-dimensional (r,z) 3-velocity (v_r, v_z, v_ϕ) dynamics for all species; detailed collision physics between charged particles and neutrals and the ability to represent multiple smooth (not stair-stepped) electrodes of arbitrary shape and voltage whose surfaces may be secondary-particle emitters (H^- and e^-). The status of this development is discussed in terms of its physics content and current implementation details.

PACS: 52.65.-y, 52.65.Pp, 52.65.Rr, 52.80.Vp, 29.25.Ni

Key words: Negative hydrogen ion source simulation, particle-in-cell with Monte Carlo collisions, low temperature plasma simulation.

1 Introduction

Ion source technology poses challenging problems both in experiments and simulations. These problems are substantially important as in many situations the output and quality of the produced beam determine much of the performance of complete accelerator systems. The relative complexity of ion sources usually means that *ad hoc* modeling may suffer from severe limitations. Fully kinetic representation offers the promise of studying

*Corresponding author. *Email addresses:* edcg@lanl.gov (E. Chacon-Golcher), kevin.j.bowers@ieee.org (K. J. Bowers)

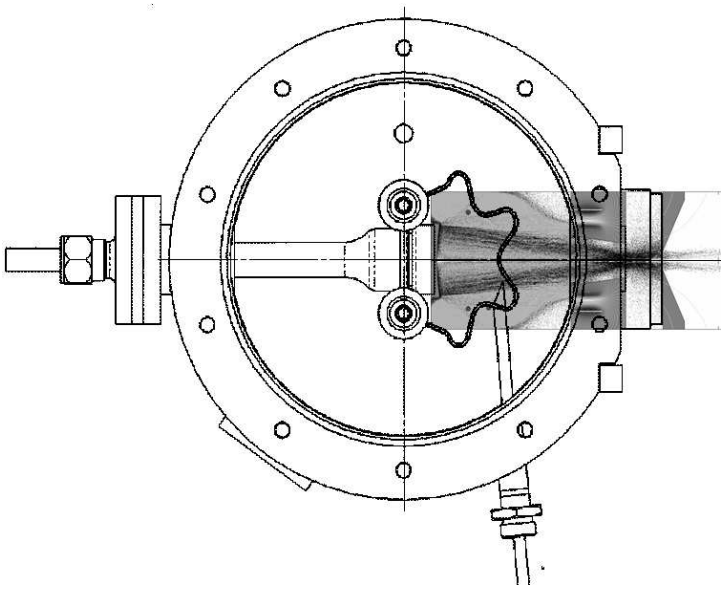

Figure 1: Composite figure showing the plasma components in the simulation region over a lateral drawing of the ion source. Shown: filaments, Cs dispenser, converter and repeller. The 3-dimensional quality of the problem has been simplified to 2 dimensions, r and z. The z coordinate is the horizontal axis of the rectangular simulation region shown, while the r coordinate is the vertical axis measured from the center of the emitting electrode. The figure shows the actual rectangular simulation region with its mirror image reflected on the z axis to suggest the cylindrical symmetry.

phenomena without full *a priori* knowledge of the myriad of effects that may affect the physics of interest. A good example of an application that can be approached this way is surface-conversion negative hydrogen ion source technology. This technology is used in diverse incarnations in major spallation neutron facilities around the world, among other applications. Both, the current output and the beam emittance of these sources impose hard limits on what can be achieved at the target end of the accelerator.

The ion source we are studying needs some description in order to provide adequate context to the reader. A blueprint of the ion source is shown in Fig. 1, with an overlay of the type of simulations described in this paper.

The ion source operates as follows: within a magnetic multicusp cylindrical chamber, a plasma discharge is initiated in a tenuous (3 to 5 mtorr) hydrogen atmosphere by incandescent tungsten filaments that are pulsed at a voltage between -100 and $-200V$. The arc produced by the filaments initiates and sustains a cascade of ionizations which form the plasma discharge. In addition to this, an external cesium oven delivers through a tube (shown in the figure) a continuous but small flow of atomic Cs.

The cesium deposits in cold surfaces all throughout the chamber. Of particular interest is the surface of a negatively biased molybdenum electrode known as the converter. This is located close to the center of the chamber, as shown in the figure. When the cesium deposits on this surface, the metal's work function is lowered and its propensity to lend electrons to adsorbed hydrogen atoms is greatly enhanced. The negative hydro-

gen ions thus formed can be knocked off by the impingement of positive ions, which are accelerated into the converter due to its potential relative to the plasma. The ions that are sputtered off traverse the high-voltage sheath (the converter bias is on the order of $-300V$), through the plasma and into a magnetic field-dominated region determined by the *repeller*. The magnetic field is intended to limit the flow of electrons into the ion source outlet. After this region, there is a short drift section which leads into the first acceleration gap and into the linac.

This brief description ought to suggest the variety of phenomena that come into play and may influence the beam output and emittance: interplay between plasma production, cathode bombardment by ions, sheath formation, beam production and propagation through plasma, ion destruction processes, diffusion of multiple species in magnetic fields and possible zones of insufficient neutralization with subsequent beam blow-up. These are the phenomena for which understanding is sought, in order to produce the visualizations and insights that may allow re-designs and improvements of this technology.

In the following pages we present an extensive update on the efforts to study this technology through the PIC-MCC method. We aim at providing more extended details than in earlier reports on this work [2, 3]. We discuss the general structure and features of the code, the physics content, results and present limitations.

2 Program organization

The program has a conventional structure, as summarized in Fig. 2. A simulation may be initialized from a neutral background hydrogen gas or from a pre-loaded plasma configuration. In any case, electrons that are emitted at the surface of the filaments initiate or sustain the plasma discharge. In the following subsections we discuss the details of every main step in the figure, such as the field calculation routines, the particle advance, boundary conditions and the Monte Carlo Collisions package.

2.1 Particle dynamics and the equations of motion

The equations of motion for all the particles have been derived from a Lagrangian formulation for a charged particle in an electromagnetic field in cylindrical coordinates:

$$L(r,z,\dot{r},\dot{z},\dot{\phi}) = \frac{1}{2}m\left(\dot{r}^2+\dot{z}^2+r^2\dot{\phi}^2\right) - q\Phi(r,z) + qr\dot{\phi}A_\phi(r,z). \tag{2.1}$$

Since ϕ is cyclical, its associated canonical momentum,

$$p_\phi = mr^2\dot{\phi} + qrA_\phi,$$

is strictly conserved. This property is assigned to each particle when created and can only be changed during collisional processes. With p_ϕ as a constant of the motion, the

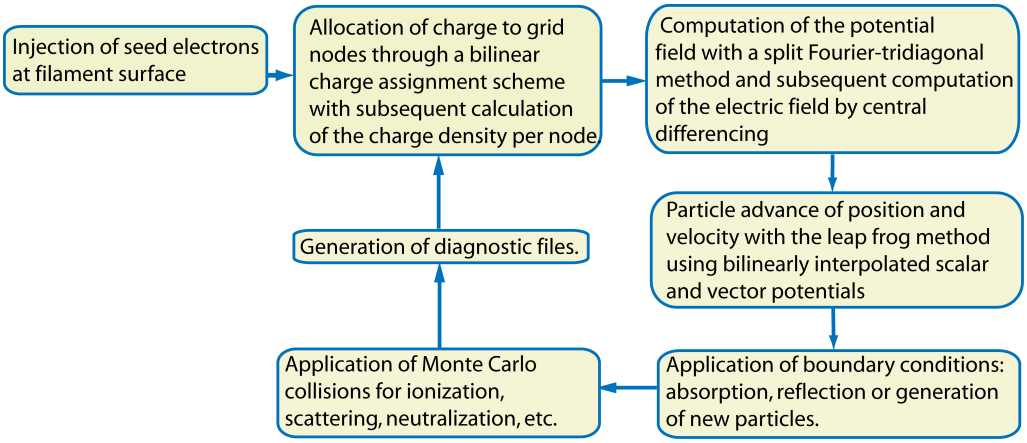

Figure 2: Flow chart of the particle-in-cell program discussed in these pages.

equations of motion are:

$$\frac{d}{dt}v_z = -\frac{\partial}{\partial z}\left[-\frac{qp_\phi}{m^2}\left(\frac{A_\phi(r,z)}{r}\right)+\frac{q}{m}\Phi(r,z)+\frac{1}{2}\left(\frac{q}{m}\right)^2 A_\phi^2(r,z)\right], \tag{2.2}$$

$$\frac{d}{dt}v_r = \frac{p_\phi^2}{m^2}\left(\frac{1}{r^3}\right)-\frac{\partial}{\partial r}\left[-\frac{qp_\phi}{m^2}\left(\frac{A_\phi(r,z)}{r}\right)+\frac{q}{m}\Phi(r,z)+\frac{1}{2}\left(\frac{q}{m}\right)^2 A_\phi^2(r,z)\right]. \tag{2.3}$$

This scheme displays several convenient properties. For example, it is fully explicit; furthermore, the use of the magnetic vector potential eliminates the need for a Boris rotation during the push, and lastly, note that the quantity in square brackets is an effective potential which can be computed at the beginning of the push for every particle species, thus reducing the number of operations per push.

The integration of the equations of motion has been implemented with the *leap-frog* method. The fields felt by a particle are interpolated from a regular grid using a momentum conserving bilinear interpolation.

2.2 Plasma chemistry model

As mentioned before, these simulations can be started out by providing an input plasma with defined characteristics or from a neutral hydrogen gas background. Since the desired beam and plasma configuration is obtained by a steady-state condition, it is more convenient to use the former method for start-up and avoid the time that it takes to build up the plasma. Nevertheless, even the pre-loaded plasma needs to be sustained by a collection of ionization, excitation and destruction reactions which occur regardless of the start-up method. The plasma model we have implemented is by no means exhaustive; it aims at providing a stepping stone towards a more realistic description of the plasma. However, it fulfills our requirements of self-consistently creating multiple ion species,

of having different thermal populations and of arriving at a stable plasma configuration with the values of density and plasma potential that match the experimental measurements.

The plasma chemistry model implemented at present is based on the *null collision* method, as described in reference [11], as such it only includes collisions between charged and neutral particles, which are effectively treated as a uniform fluid. While limited, this approach has the strength of being an accurate representation of what can be expected from analytical considerations. The fundamental premise of the method, that of the constancy of the number density of the neutral gas background, is preserved since at most, only about 1% of the gas is ionized. Five types of reactions have been included: ionization reactions, rotational and vibrational molecular excitations, charge exchange reactions, H_3^+ creation and H^- destruction reactions. In the following sections we sketch the main features, assumptions and simplifications we have applied in order to aid the interested reader in reproducing or improving on this work. All cross section data that has been used in this work has been obtained from [10]. This reference presents a wide diversity of reactions with their corresponding reaction energies where applicable.

2.2.1 Ionization reactions

Three reactions of this type have been included in the model. These are listed in Eqs. (2.4) to (2.6):

$$e^- + H_2 \rightarrow H_2^+ + 2e^-, \tag{2.4}$$

$$e^- + H_2 \rightarrow H^+ + H + 2e^-, \tag{2.5}$$

$$e^- + H \rightarrow H^+ + 2e^-. \tag{2.6}$$

Eq. (2.5) has two main channels in which it can occur. In one channel, the ion fragments are born "cold" as the incident electron may only provide enough energy for the ionized molecule to dissociate. In the second channel, an intermediate molecular excited state is created which then dissociates giving the fragments up to a few tens of electronvolts to share among them. The cross section information which the authors had available did not distinguish between these two different channels. A Monte Carlo procedure was thus devised to account for the ratio of energetic H^+ to "cold" fragments. Data for this procedure has been taken from [1]. When this reaction is selected to occur by the *null collision* method, a probabilistic approach then decides which channel is taken by considering the available electron energy. If energetically allowed, and if selected, the "energetic fragment" channel is applied. The available energy for the fragments is dependent on the energy of the induced excited state in the hydrogen molecule. It can be seen from energy diagrams for the hydrogen molecule that there is a relatively wide range of values that the excited molecule can have (see an example of such diagrams in [6]), depending on the internuclear distance at the moment of dissociation. The internuclear distance will fall in a gaussian distribution around the average distance. In our implementation, for the sake

of simplicity, we have assumed that the internuclear distance is uniformly distributed around the mean, and from there the energy of the resulting excited state is computed.

In general, to compute the ionization reactions, two distinct neutral background fluids must be present in the simulation: atomic and molecular hydrogen. In our computations, the neutral atomic density has been set at 1% of the density of the molecular gas.

Following the practice described in reference [11], the fundamental assumption in the modeling of this kind of reaction is that the target is assumed stationary with respect to the incident electron. All the electron–neutral collisions have been treated with the following relation to compute the scattering angle of the incident electron:

$$\cos(\chi) = \frac{2+\varepsilon-2(1+\varepsilon)^{r_1}}{\varepsilon}, \tag{2.7}$$

where χ is the angle between the incident and scattered velocities of the incident electron, ε is the energy of the incident electron and r_1 is a uniformly distributed random number. In work by other researchers, this formula has been applied to oxygen, argon and helium (see references [8, 9, 11]). Note also that [8] takes ε to represent the electron energy after the scattering. In this work we subscribe to the meaning in [11]. While not capable of providing the specific, fine-tuned scattering features of each species, formula (2.7) does display the general expected properties of nearly isotropic scattering at low electron energies and forward scattering at higher energies.

To compute the energy of the ejected electron in the ionization process we use the empirical formula

$$\varepsilon_{ej} = B \arctan\left(\frac{(\varepsilon-\varepsilon_{ionization})}{2B}\right) r_2, \tag{2.8}$$

where the formula has been taken from [11] and the shape parameter applicable to molecular hydrogen ($B=8.3$) from [7]. $\varepsilon_{ionization}$ is the ionization energy for the reaction and ε_{ej} is the energy of the ejected electron, r_2 is a uniformly distributed random number.

The ionization reaction is thus treated as a collision between electrons, with no energy transfer to the resulting ion. Once the ionization energy is subtracted from the incident electron energy, the collision between the incident and the ejected electrons is treated as an elastic collision in which the available energy is distributed as mentioned above and the scattering angle of the ejected electron is computed with momentum conservation. The resulting ion is created with a velocity picked from an isotropic Maxwellian distribution at the temperature of the neutral gas present in the ion source.

2.2.2 Rotational and vibrational molecular excitation reactions

Molecular excited states induced by electron collision have been included. These are listed in Eqs. (2.9) through (2.18). An additional excitation reaction induced by collision

with a proton has been included and is represented by Eq. (2.19):

$$e^- + H_2 \rightarrow H_2(J=0 \rightarrow 2) + e^-, \tag{2.9}$$
$$e^- + H_2(\nu=0) \rightarrow H_2(\nu=1,2,3) + e^-, \tag{2.10}$$
$$e^- + H_2 \rightarrow H_2(b\ ^3\Sigma_u^+) + e^-, \tag{2.11}$$
$$e^- + H_2 \rightarrow H_2(B\ ^1\Sigma_u^+) + e^-, \tag{2.12}$$
$$e^- + H_2 \rightarrow H_2(C\ ^3\pi_u^+) + e^-, \tag{2.13}$$
$$e^- + H_2 \rightarrow H_2(D\ ^1\pi_u^+) + e^-, \tag{2.14}$$
$$e^- + H_2 \rightarrow H_2(D'\ ^1\pi_u^+) + e^-, \tag{2.15}$$
$$e^- + H_2 \rightarrow H_2(B''\ ^1\Sigma_u^+) + e^-, \tag{2.16}$$
$$e^- + H_2 \rightarrow H_2(c\ ^3\pi_u) + e^-, \tag{2.17}$$
$$e^- + H_2 \rightarrow H_2(a\ ^3\Sigma_g^+) + e^- \text{ and} \tag{2.18}$$
$$H^+ + H_2(\nu=0) \rightarrow H^+ + H_2(\nu=1,2,3). \tag{2.19}$$

The excitation reactions by electron bombardment have been treated in analogous way with the ionizations described in the previous subsection, with the difference that the energy of the scattered electron has been decreased only by the energy of the corresponding excitation. The excitation induced by protons is treated differently. In this case the projectile and the target are of very similar mass, thus the target can not be assumed to be stationary. The collision is furthermore, inelastic. For this reason, a procedure is applied that simultaneously includes the effects of the scattering itself and of the loss due to the reaction energy. We follow the common practice of doing the computations in the center-of-mass frame. The velocity of the target particle is taken from a 3-velocity Maxwellian at the temperature of the neutral gas. Assuming an isotropic scattering in the center-of-mass frame, we compute the ratio ρ of the relative velocity between projectile and target before and after the collision. This is given by

$$\rho = \frac{m_p}{m_t}\left(1 - \frac{m_p + m_t}{m_t}\frac{Q}{E_{inc}}\right)^{-\frac{1}{2}}, \tag{2.20}$$

where m_p and m_t are the masses of the projectile an target respectively, Q is the reaction energy and E_{inc} is the incident (projectile) energy in the CM frame. This is used to compute the scattering angle in the laboratory frame:

$$\cos(\chi) = \frac{\cos(\Theta) + \rho}{\sqrt{1 + 2\rho\cos(\Theta) + \rho^2}}, \tag{2.21}$$

where Θ is the scattering angle in the CM frame (much of the nomenclature in this subsection follows that of [4]), which as mentioned, has been taken from an isotropic distribution. The velocity components of the scattered particle can be scaled by knowing the

ratio of the scattered particle's energy to its incident energy:

$$\frac{v_1^2}{v_0^2} = \left(\frac{\mu}{m_2\rho}\right)^2 \left(1+2\rho\cos(\Theta)+\rho^2\right), \tag{2.22}$$

where v_1 is the energy of the scattered particle, v_0 the incident energy and μ the reduced mass of the system. Like with the ionization reactions, the excited neutral molecules or neutral fragments are not tracked.

2.2.3 Charge exchange reactions

The charge exchange reactions included in Eqs. (2.23) and (2.24) are computed in a frame of reference in which the target is stationary. Once again, the velocity components of the neutral particle are selected from Maxwellian distributions at the neutral gas temperature. If the reaction is selected, the velocity components of the incident and target particle are switched and then transferred back into the laboratory frame:

$$H^+_{fast} + H^0_{slow} \rightarrow H^+_{slow} + H^0_{fast}, \tag{2.23}$$

$$H^+_{2\ fast} + H^0_{2\ slow} \rightarrow H^+_{2\ slow} + H^0_{2\ fast}. \tag{2.24}$$

2.2.4 H_3^+ creation reaction

Creation of the H_3^+ ions is treated as an inelastic scattering of H_2^+ on a hydrogen molecule, in analogous way of the treatment of Eq. (2.19), with the difference that the reaction described by Eq. (2.26) is exothermic with a Q of 1.7 eV. Furthermore, since the "scattered" particle is now a different species, this must be taken into account in the energy an momentum conservation equations. For instance, Eq. (2.22) becomes:

$$\frac{v_1^2}{v_0^2} = \left(\frac{m_1}{m_3+m_4}\frac{1}{\rho}\right)^2 \left(1+2\rho\cos(\Theta)+\rho^2\right), \tag{2.25}$$

where m_1 and v_1 are the mass and speed of the incident molecular ion, m_3 is the mass of the resulting hydrogen atom and m_4 and v_1 are the mass and speed of the produced H_3^+ ion:

$$H_2^+ + H^0_{2\ slow} \rightarrow H_3^+ + H^0. \tag{2.26}$$

2.2.5 H^- destruction reaction

Destruction of negative hydrogen ions is an important process as the ion losses can become quite significant within an ion source. There are two main contributors to the destruction of H^- ions: collisions with neutrals and collisions with electrons. In the present form of the implementation, only collisions with neutrals are included. This is still regarded as the dominant loss mechanism due to the relatively high number density of neutral particles. In the higher end of the plasma density values we are exploring, the

contribution of electron collisions may approach the contribution of the neutral hydrogen. Therefore the overall destruction may in some cases be underestimated by up to 50%.

The implementation of the reaction (2.27) simply destroys the negative hydrogen as all the detailed collision dynamics occur between (non-tracked) neutral particles. It has been assumed that the ejected electron is created with an energy equal to the binding energy to the H_3^+ ion, i.e. 0.85 eV and with a velocity selected from an isotropic distribution:

$$H^- + H_2 \rightarrow H^0 + H_2 + e^-. \tag{2.27}$$

2.3 Solution of electric and magnetic fields

The electric potential and magnetic vector potential are represented on a regular grid. Given that the magnetic field is static, its solution is carried out only once at the beginning of the simulation. Due to the axial symmetry of our problem only one component (A_ϕ) is needed. The vector potential is computed from the contributions of a set of current-carrying rings on the surface of the magnet. The magnetic element included is a ring magnet within the *repeller* electrode the ion source.

The solution of the electrostatic fields must be computed every time-step, hence the performance of this segment of the program is critical. A split FFT/tridiagonal approach is used to solve for the electrostatic field produced by a collection of charges. This yields a "homogeneous" solver in the sense that zero potential values are forced at the edges of the solution region with exception of the axis of symmetry. The stencils used at this step are derived by substituting the inverse *sine* transform formula for ϕ and ρ into the discretized Poisson's equation, thus yielding the following tridiagonal system of equations

$$\begin{aligned}\left(\frac{1}{(\Delta r)^2}+\frac{1}{2r\Delta r}\right)\widetilde{\phi}_{r+1,k}-\left(\frac{2}{(\Delta r)^2}+\frac{4}{(\Delta z)^2}\sin^2\left(\frac{\pi k}{2N_z}\right)\right)\widetilde{\phi}_{r,k}\\ +\left(\frac{1}{(\Delta r)^2}-\frac{1}{2r\Delta r}\right)\widetilde{\phi}_{r-1,k}=-\frac{\widetilde{\rho}_{r,k}}{\epsilon_0},\end{aligned} \tag{2.28}$$

while at the axis of symmetry

$$\frac{4}{(\Delta r)^2}\widetilde{\phi}_{1,k}-\left(\frac{4}{(\Delta r)^2}+\frac{4}{(\Delta z)^2}\sin^2\left(\frac{\pi k}{2N_z}\right)\right)\widetilde{\phi}_{0,k}=-\frac{\widetilde{\rho}_{0,k}}{\epsilon_0}. \tag{2.29}$$

In Eqs. (2.28) and (2.29), Δr and Δz are the grid sizes in the r and z directions respectively, N_z is the number of cells in the z direction, and $\widetilde{\phi}$ and $\widetilde{\rho}$ are the sine-transformed values of the potential and charge density. Thus the homogeneous Poisson equation is solved by sine transforming the charge density ρ, solving the resulting tridiagonal linear system above and finally inverse-transforming the result. This yields a quite fast solution.

2.3.1 Implementation of smooth electrode boundaries

In the present implementation, arbitrary, mixed boundary conditions (Dirichlet and Neumann) can be set anywhere on the solution region, including the true positions of physical boundaries, specifically, the electrode structures inside the solution region needed to describe the geometry in the ion source. This is implemented through the capacity matrix method [5]. After the homogeneous solution of Poisson's equation is found, charge is allocated at specific nodes to enforce general conditions of type

$$\gamma = \alpha\phi + \beta\hat{n}\cdot\nabla\phi, \tag{2.30}$$

where α and β are constants and $\hat{n}$ is the normal to a surface of interest. Once this "surface charge" is allocated, a second application of the homogeneous solver yields the desired, complete solution. This solution method is direct and fast—permitting simulations with hundreds of thousands of timesteps in reasonable time.

Solution of Poisson's equation on a regular grid is a common method used in other codes and provides the advantages of speed and knowledge of error bounds. A drawback is the difficulty of representing boundaries that are not parallel to the radial axis or longitudinal axis or not aligned with the grid. The presence of stair-stepped boundaries (following grid lines) is a concern when secondary emission from a surface is considered. In our application, unwanted artifacts are introduced when non-smooth surfaces are used. Such stair-stepped surfaces have the wrong surface area and also involve more obvious errors such as electric fields that are non-normal with respect to the desired boundary.

Smoothness in the representation of the internal surfaces is achieved as follows. The main idea of the capacity matrix method is to relate the potential values on a set of points to the allocated charge on another (possibly the same) set of points through a matrix equation. In our current implementation, we exploit the possibility of choosing two different sets of points. One set of points is where the boundary condition will be enforced and resides precisely on the physical boundary whose smooth representation is desired. The other set is where the required surface charge must be allocated and is strictly interior to the electrode structure but close to its surface. In this way, the physical content of the solution is preserved, simulating the distribution of surface charge needed to ensure the right equipotential at the (smooth) electrode surface. A schematic of this is shown in Fig. 3. In the figure, the rectangular grid is divided by a physical boundary that represents the true electrode surface. It is desired to enforce an equipotential on this boundary. The algorithm first selects a set of "edge nodes", interior to the electrodes but adjacent to at least one free space node. Each of these nodes (represented by full circles) is associated with a point on the logical boundary. By proper allocation of charge on the edge nodes, it is possible to enforce the desired value of the potential on the electrode surface.

The algorithm that selects the points on the logical boundary considers all the possible cases that may arise regarding the number of "free space" nodes in the vicinity of an edge node. Fig. 4 summarizes the cases that may be encountered and where the algorithm

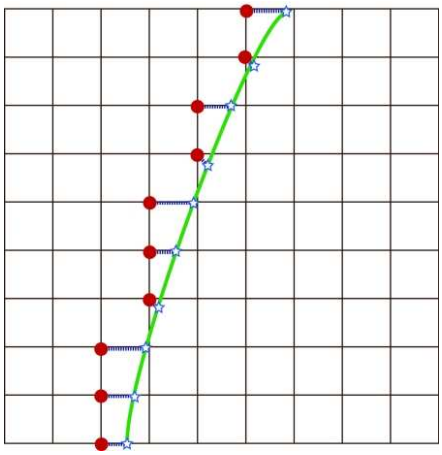

Figure 3: Schematic of the pairing between points on the physical boundary (marked with stars) where the potential value is enforced and the corresponding electrode edge node where the surface charge is allocated (marked with full circles).

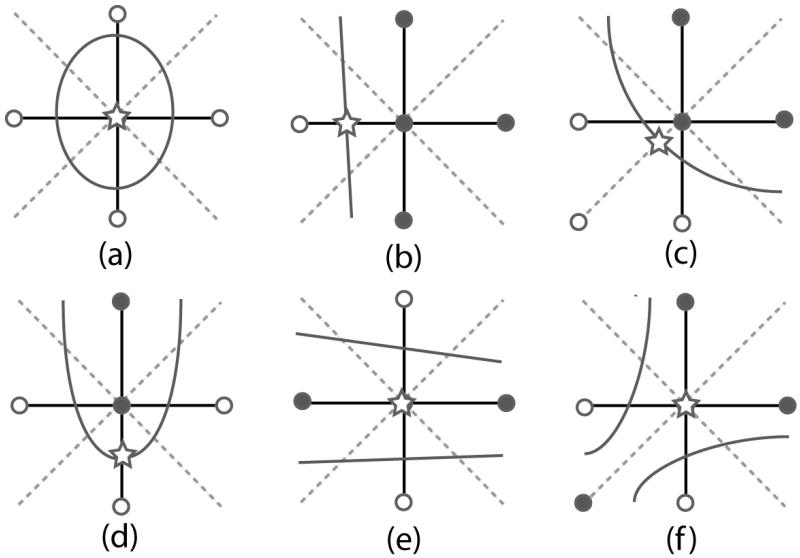

Figure 4: Set of cases that may arise in terms of pairing an edge node (center node in each case) to a point on the logical boundary (starred). The smooth lines represent the position of the logical boundary. Empty circles lay outside of the electrode on the "free space" region while full circles are nodes within the electrodes. Note that in some cases, the point where the voltage is enforced is not directly on the logical boundary. All cases encountered can be reduced to one of the above cases.

decides to enforce the potential. There are a total of 2^4 possible cases. In some cases, the point where the potential value is enforced is not directly on the logical boundary, but these are infrequent, usually related with very narrow electrodes (narrower than the cell size), knife-edges and similar shapes. This algorithm provides satisfactory behavior for the geometries of interest in typical ion sources and "ion gun" simulation geometries.

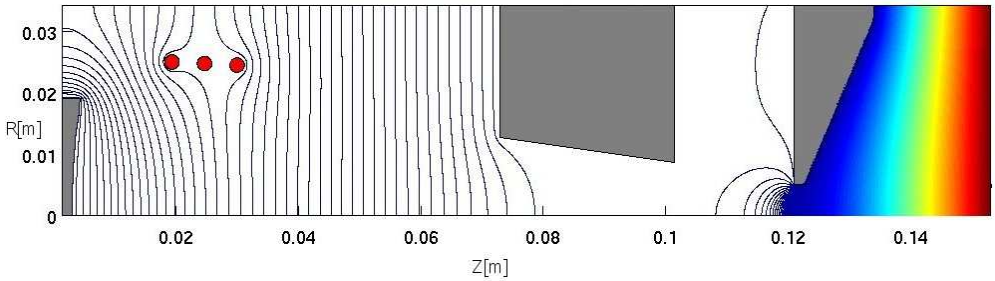

Figure 5: Plot of equipotentials when no particles are present. Neumann boundary conditions applied to top and left edges that intercept the plasma.

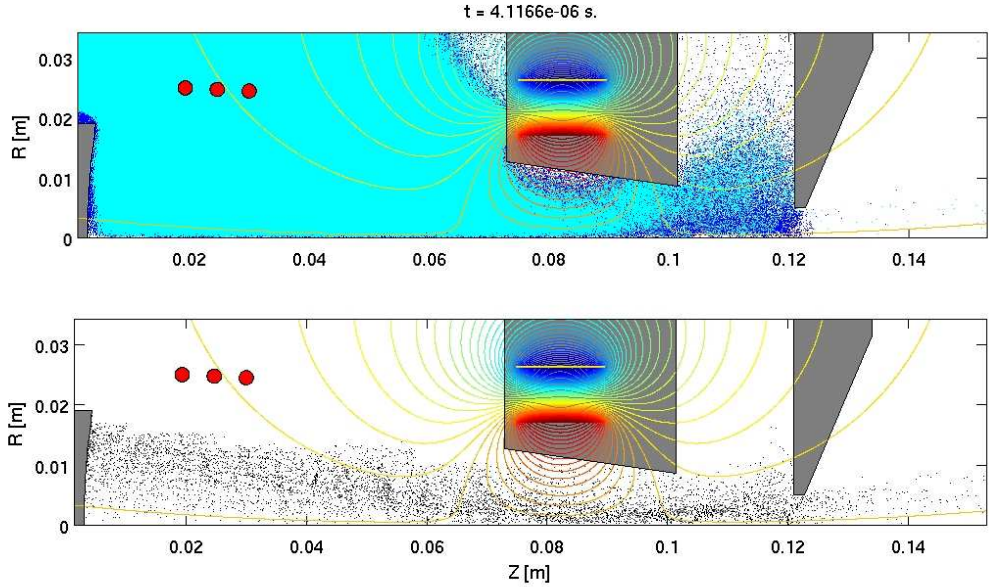

Figure 6: Configuration space of the different plasma species at 636,000 steps. Top: electrons (light blue) and positive ions (dark blue) conform the bulk plasma. Bottom: negative hydrogen ions.

3 Results & discussion

One of the problems encountered when a full discharge has been simulated (i.e., when the simulation is brought up from a neutral gas) has been an insufficient thermalization of the plasma electrons. This has posed problems regarding the achievement of the right plasma potential value, apart from the effects on the particle dynamics. The way in which this has been addressed involves two steps. The first has been to include a Neumann condition at the edge of the solution region that intercepts the plasma bulk. In this way, the potential at this edge is allowed to float. Without this, it would be necessary to fix the voltage of such boundary at some value, with the subsequent formation of sheaths all along. The Neumann condition eliminates gradients normal to these edges. Fig. 5 shows

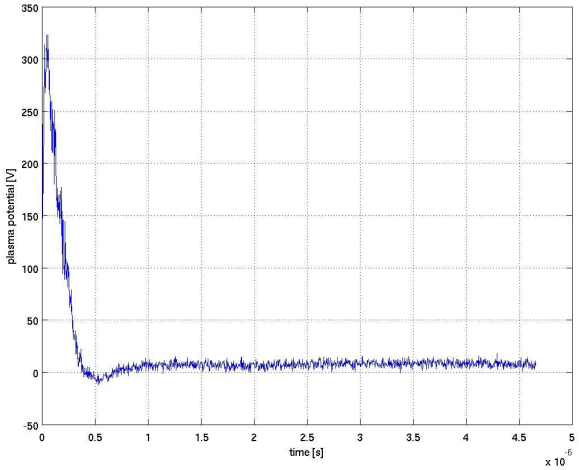

Figure 7: Time evolution of the plasma potential during the simulation. Initial surge caused by the pre-loaded plasma configuration, inconsistent with the equilibrium configuration.

the Neumann conditions at the plasma-intercepting edges. The second step has been the addition of a *refluxing* condition for the electrons at these edges. This means that when electrons cross this boundary they are reflected back into the solution region. The important fact here is that the electrons are reflected with a thermal velocity. Thus the plasma edge becomes in fact a source of thermal electrons. If a uniform thermal plasma is loaded, it will replenish itself through this refluxing condition. In effect what is addressed here is the discrepancy between the electron loss area between the simulation and the experimental device. It is possible to mimic here the effect of a plasma density profile by making the refluxed electrons have a fraction of the charge than the exiting one. This has been also applied in our simulations. At the same time, the ion population is replenished by the ionization reactions induced by filament-born electrons, which as mentioned before, do not completely thermalize. This results in two electron populations, which is a desired outcome, as this is what is experimentally observed. The positive ions are not refluxed, so the outer edges are a loss region for the ions.

Fig. 6 shows a representative snapshot of the simulations in a steady-state. Note the formation of the sheath around the converter electrode and the diffusive sheaths in the magnetic field region. The area between the last two electrodes has been identified as an area of possible beam losses due to beam expansion. Studies are underway to explore the effects of different magnet field strengths and configurations. Fig. 7 shows the plasma potential plot over time. A "jump" in the plasma potential can be seen at the beginning of the simulation. This is due to the initial, uniform loading of the plasma species which are initially "shocked" away from the negatively biased electrode, afterwards, the system relaxes to a more stable configuration. Stability of the plasma potential value was an issue in earlier reports on this work. The fine tuning of the injected electron current and the ionization cross sections (in both cases within experimental uncertainty) has been found to be an important aspect of achieving the desired stability at the desired parameters.

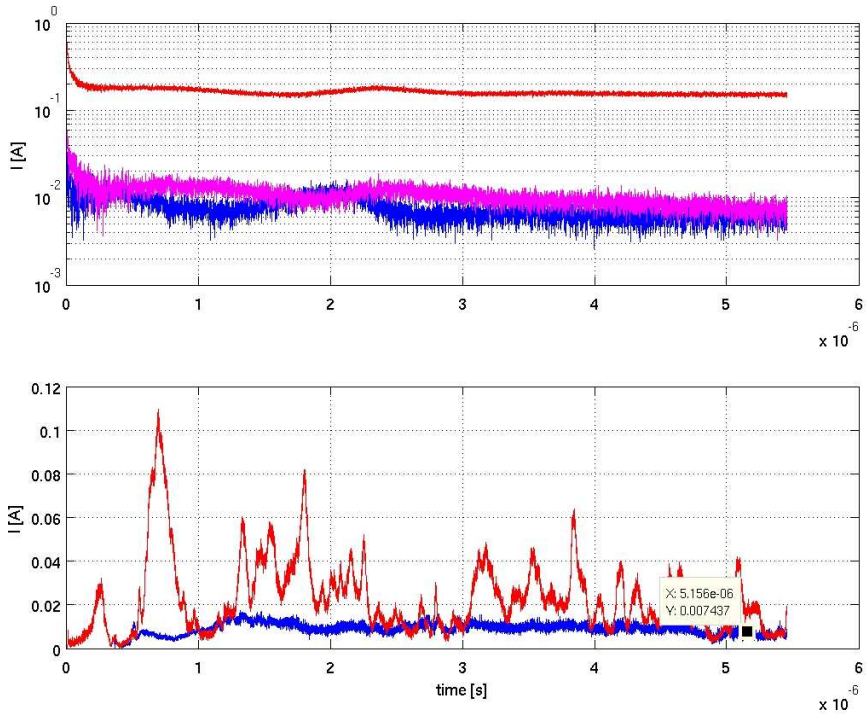

Figure 8: Top: positive ion contribution to the converter current. The highest contributor is H_2^+. Bottom: Currents on exit of electrons (red) and negative hydrogen (blue). Slight decrease makes evident a slow decrease in the plasma density. High variability of the electron current can be partially ascribed to streaming instabilities.

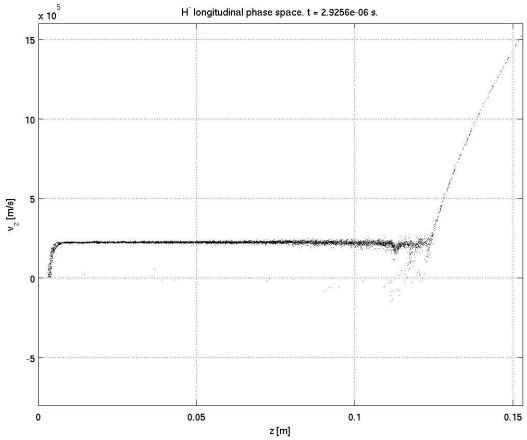

Figure 9: Longitudinal phase space plot of the beam showing areas of acceleration and drift. Note formation of instabilities just before the last acceleration.

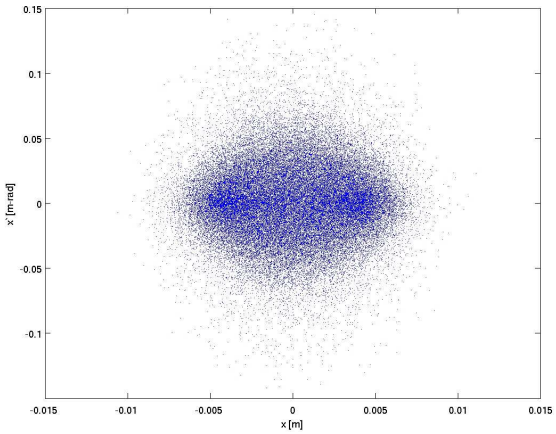

Figure 10: Phase space plot of beam on exit of the simulation region. Some hollowness can be observed. $\epsilon_0 = 0.15\pi - mm - mrad$.

Fig. 8 shows the currents measured on the converter due to impinging positive ions and the current measured on exit of the source due to electrons and negative hydrogen. This allows comparisons with the measured values in the experiments. Converter

currents shown in the figure, as well as the negative hydrogen currents suggest an underdense plasma in this case, due to the magnitude of the H^- current and also a dropping plasma density, due to the dropping current. The high variability of the electron current is obvious. In the simulations it is easy to see that there are various opportunities for streaming instabilities to form. The clearest ones are the filament electrons and the converter electrons and H^- as they traverse the plasma. The electron current variability can be correlated with the formation of instabilities. Fig. 9 shows a longitudinal phase-space plot of the negative hydrogen. It shows the areas of acceleration and drift very clearly. Of note is the presence of waves (due to streaming) which cause the formation of electron "pockets" and thus cause the variability of the electron current. To what extent the beam emittance is affected by these phenomena is under study.

Finally, Fig. 10 shows a sample emittance plot of the beam produced by the simulation. Some hollowness can be seen. The phase space plot has a normalized emittance of 0.15 $\pi-mm-mrad$. This value is in the range of the experimental values observed, nevertheless, since the measured current corresponding to this plot was 50% lower than expected, it is possible that the simulation is overestimating the mechanisms for emittance growth at this point. Present work is also aimed at understanding and addressing this.

Acknowledgments

This research is supported by the US Department of Energy through contract DE-AC52-06NA25396.

References

[1] W. BLEAKNEY, *The ionization of hydrogen by single electron impact*, Physical Review, 35 (1930), pp. 1180–1186.

[2] E. CHACON-GOLCHER AND K. J. BOWERS, *A particle-in-cell gun code for surface-converter h^- ion source modeling h^- ion source*, American Institute of Physics Proceedings Series, 925 (2006), p. 306.

[3] E. CHACON-GOLCHER AND K. J. BOWERS, *Two-dimensional, three-velocity particle-in-cell with monte carlo collisions simulations of lansce's h^- ion source*, Review of Scientific Instruments, 77 (2006), p. 03A526.

[4] H. GOLDSTEIN, *Classical Mechanics*, Addison-Wesley Series in Physics, Addison-Wesley Publishing Company, Inc., 1980.

[5] R. W. HOCKNEY AND J. EASTWOOD, *Computer Simulation Using Particles*, Institute of Physics Publishing Ltd., London, 1988, p. 215.

[6] M. LIEBERMAN AND A. LICHTENBERG, *Principles of Plasma Discharges and Material Processing*, John Wiley and Sons, Inc., New York, NY, 1994.

[7] C. OPAL, W. PETERSON, AND E. BEATY, *Measurements of secondary-electron spectra produced by electron impact ionization of a number of simple gases*, Journal of Chemical Physics, 55 (1971), pp. 4100–4106.

[8] M. SURENDRA AND D. GRAVES, *Electron heating in low-pressure rf glow discharges*, Applied Physics Letters, 56 (1990), pp. 1022–1024.

[9] M. SURENDRA, D. GRAVES, AND G. JELLUM, *Self-consistent model of a direct-current glow discharge: Treatment of fast electrons*, Physical Review A, 41 (1990), pp. 1112–1125.

[10] H. TAWARA, Y. ITIKAWA, Y. ITOH, T. KATO, H. NISHIMURA, S. OHTANI, H. TAKAGI, K. TAKAYANAGI, AND M. YOSHINO, *Atomic data involving hydrogens relevant to edge fusion plasmas*, Tech. Report IPPJ-AM-46, Institute of Plasma Physics, Nagoya University, Nov. 1988.

[11] V. VAHEDI AND M. SURENDRA, *A monte carlo collision model for the particle-in-cell method: applications to argon and oxygen discharges.*, Computer Physics Communications, 87 (1995), pp. 179–198.